Heliyon 8 (2022) e10682

Contents lists available at ScienceDirect

Heliyon

journal homepage: www.cell.com/heliyon

Research article

# Validation of Monte Carlo-based calculations for megavolt electron beams for IORT and FLASH-IORT

Graeme L. Lazarus [a], Déte van Eeden [b,*], Frederik CP. du Plessis [b]

[a] University of Kwazulu-Natal, School of Clinical Medicine, College of Health Sciences, Durban, 4013, South Africa
[b] Department of Medical Physics, University of the Free State, Bloemfontein, 9300, South Africa

ARTICLE INFO

*Keywords:*
Electron beam
Intra-operative radiation therapy
FLASH therapy
Monte Carlo

ABSTRACT

In Intra-Operative Radiation Therapy (IORT) the tumour site is surgically exposed and normal tissue located around the tumour may be avoided. Electron applicators would require large surgical incisions; therefore, the preferred mechanism for beam collimation is the IORT cone system. FLASH radiotherapy (FLASH-RT) involves the treatment of tumours at ultra-high dose rates and the IORT cone system can also be used. This study validates the Monte Carlo-based calculations for these small electron beams to accurately determine the dose characteristics of each possible cone-energy combination as well as custom-built alloy cutouts attached to the end of the IORT cone. This will contribute to accurate dose distribution and output factor calculations that are essential to all radiation therapy treatments. A Monte Carlo (MC) model was modelled for electron beams produced by a Siemens Primus LINAC and the IORT cones. The accelerator was built with the component modules available in the BEAMnrc code. The phase-space file generated by the BEAM simulation was used as the source input for the subsequent DOSXYZnrc simulations. Percentage Depth Dose (PDD) data and profiles were extracted from the dose distributions obtained with the DOSXYZnrc simulations. These beam characteristics were compared with measured data for 6, 12, and 18 MeV electron beams for the IORT open cones of diameters 19, 45, and 64 mm and irregularly shaped cutouts. The MC simulations could replicate electron beams within a criterion of 3%/3 mm. Applicator factors were within 0.7%, and cone factors showed good agreement, except for the 9 mm cone size.

Based on the successful comparisons between measurement and MC-calculated dose distributions, output factors for the open cones and for small irregularly shaped IORT beams, it may be concluded that the Monte Carlo based dose calculation could replicate electron beams used for IORT and FLASH-IORT.

## 1. Introduction

Conventional external beam radiation therapy (EBRT) involves using medical linear accelerators to target tumours with a dose of radiation. For an effective dose to be delivered to deep-seated tumours, higher doses of x-rays are delivered to normal tissues or internal organs located around the tumour. This results in an unfavourable therapeutic ratio, that describes the correlation of tumour control probability (TCP) and normal tissue complication probability (NTCP) [1]. A TCP of ±95%, but at the cost of a NTCP of 50% is often regarded as being an unacceptable risk for the normal tissue [2].Ways to reduce the damage to normal tissue has always been a popular topic for radiotherapy research.

One of the techniques is to use Intra-Operative Radiation Therapy (IORT), where the tumour site is surgically exposed. It allows a single dose of radiation to be administered directly to the tumour whilst displacing normal tissue and organs [3]. IORT treatment has been described for rectal cancer, soft tissue sarcoma, pancreatic cancer and also for the conservative therapy of breast cancer [4, 5, 6]. During the last years, recommendations have been published on the IORT with electrons in breast cancer [7], borderline-resected pancreatic cancer [8], soft tissue sarcoma [9] and rectal cancer [10]. IORT treatment has also been described for pediatric Ewing sarcoma [11] and gynecologic malignancies [12].

IORT may also take place after partial resection of the tumour. For IORT with electron beams, normal tissue beyond the distal end of the tumour may be avoided by selecting appropriate available electron beam energy to control beam penetration. Electron beams inherently display a rapid dose fall-off and have a finite range in tissue compared with x-rays. Electron beams are more suitable than photon beams for treating superficial tumours due to their narrow build-up region. Electron beams

* Corresponding author.
*E-mail address:* vaneedend@ufs.ac.za (D. van Eeden).

https://doi.org/10.1016/j.heliyon.2022.e10682
Received 23 March 2022; Received in revised form 18 May 2022; Accepted 13 September 2022

have a dose-rate advantage over ortho-voltage x-rays meaning that tumour irradiation can be completed in a short time. In the case of EBRT, followed by surgery, the tumour cells are given time to grow before the surgery takes place.

In contrast, with IORT, the microscopic tissue remaining after resectioning the tumour is irradiated immediately after resection, preventing tumour cells from growing. Another advantage is that OARs and normal tissue may be shielded or moved out of the beam, allowing dose escalation increasing the tumour control probability to normal tissue complication probability (TCP/NTCP) ratio. The single high doses delivered in IORT avoid the tumour cells' repopulation that occurs with fractionated EBRT.

Another approach is to use FLASH radiotherapy (FLASH-RT) to reduce radiation-induced damage in healthy tissue [13, 14]. FLASH irradiation is 400-fold more rapid than conventional irradiation and can reduce radiation-induced damage in healthy tissue while keeping the tumour control unchanged. This biological effect is referred to as the FLASH effect, and the mechanism behind this phenomenon still needs to be elucidated [15]. It has been suggested that the differential response between FLASH and conventional radiotherapy may be due to the radiochemical depletion of oxygen that leads to hypoxia [16, 17, 18]. The FLASH effect has been validated by various animal models, organs and radiobiology research works [14, 19, 20, 21, 22, 23, 24]

It has been shown that an accelerator dedicated to IORT can be modified to obtain FLASH beams [25]. In a recent study, the acceptance and commissioning of an ultra-high dose rate pulsed electron beam medical linear accelerator (LINAC) was presented by using radiochromic film and ionisation chamber measurements [26].

In terms of IORT electron beam delivery, initial collimation of the electron beam is provided by the movable photon collimator jaws and multi-leaf collimators (MLC). The square-sided electron applicators that are supplied with LINACS cannot be used for IORT due to their large size ($5 \times 5$ to $25 \times 25$ cm$^2$). Even when using the smallest $5 \times 5$ cm$^2$ applicator, a large incision would have to be made to insert the applicator in close proximity with the surgically exposed tumour. Therefore, the preferred mechanism for beam collimation is the IORT cone system. The field sizes of conventional clinical LINACS also limit the clinical use of FLASH-IORT, and the IORT cone system can be utilised instead.

The circular applicators have a wide range of diameters from about 2 cm to10 cm for larger treatment areas. The cone systems are incorporated into the existing LINAC, and no modifications are necessary. The cone systems contain adaptor plates that can slide into the accessory slot of the treatment head.

Over the past years, the great majority of the IORT community has moved to dedicated mobile LINACS, provided by IntraOp [27] and SIT [28], to name a few. These devices have been intensively studied and modelled in previous studies by Monte Carlo (MC) simulations. MC simulations were used to simulate the heads of two electron accelerators dedicated to IORT to characterise the beams [29]. In another study, the dosimetric characteristics of the Liac® (SORDINA, Italy) was determined with a minimal set of dosimetric data that can be used to support the medical physicist in the commissioning phase [30]. In a previous study, MC was used for treatment planning of intraoperative electron radiation therapy (IOERT) procedure by using patient's computed tomography (CT) images [31].

This study shows new and valuable results for small fields obtained with irregular cutouts.

The IORT cone system (Radiation Products Inc.) used is described in the methods section. The following set of measurements was done to define the dose characteristics of different cone-energy combinations used during IORT and FLASH-IORT therapy: central axis percentage depth dose (PDD); beam profiles at various depths; isodose contours; surface dose estimation; absolute dosimetry, applicator (output) factors, cutout factors, air gap factors, lead transmission factors, and alloy transmission factors.

In order to determine the above characteristics, water tank measurements can be performed. These data can then be used to set up an accurate MC model for IORT electron beams. MC is any process where random sampling from probability distribution functions is used to construct solutions to problems. The application of the MC method was introduced to the field of radiation therapy in the 1970s and gave it a more acceptable alternative to solving complex transport equations analytically [32].

MC simulation of radiation transport models the interactions between radiation and matter. MC-based systems take into account the path and energy loss of all the particles in the incident beam and have become the golden standard for dose calculations [33, 34].

High-energy electrons suffer a large number of collisions and Monte Carlo have multiple scattering theories for the simulation of these particles [35]. Dominant interactions include inelastic scattering, elastic scattering, and bremsstrahlung emission. Inelastic collisions result in a loss of the incident electron's energy in the form of ionisation or the excitation of the absorber atoms. The inelastic collision for high-energy MC simulations is based on the plane-wave Born approximation (PWBA).

No kinetic energy is lost in elastic collisions; however, a very small energy loss may occur that produce a deflection in the electron's path [36]. A review of the calculation methods and experimental measurements of elastic scattering of electrons can be found in the ICRU Report 77 (ICRU 2007) [37]. Bremsstrahlung is produced in the components of the accelerator head and can be seen as a low-level dose component in the tail of the electron spectrum. The Seltzer and Berger's tables of bremsstrahlung spectra are adopted in many Monte Carlo codes [38, 39].

Therefore, it has become the gold standard for determining absorbed dose in a medium from clinical radiotherapy beams and has been extensively benchmarked [40, 41].

The motivation for this study was to set up an MC model for electron beams produced by a Siemens Primus LINAC together with the IORT cones (Radiation Products Inc.) for electron IORT treatment planning, also to be utilised for FLASH-IORT. We compared MC calculated beam characteristics with measurements for the Siemens Primus LINAC for 6, 12, and 18 MeV electron beams for the IORT open cones of diameters 19, 45, and 64 mm that also included irregularly shaped cutouts attached to the cone end to conform the shape of the beam to the treatment site.

## 2. Materials and methods

The study involves validating MC-based calculations over three stages; In stage I, we commissioned the LINAC model by comparing beam profiles and percentage depth dose curves with water tank measurements using a 10 cm $\times$ 10 cm and 15 cm $\times$ 15 cm applicator. In stage II, we model the cones used for IORT and compare beam profiles and depth dose data with water tank data. In stage III, we repeat the process for irregularly shaped intra-operative radiotherapy electron fields.

The 6, 12, and 18 MeV beams will be benchmarked in this study and will be defined as the beam set, {E}. The dimensions and material composition of the treatment head were obtained from the vendor.

### 2.1. Stage I: Monte Carlo commissioning of the linac

Central axis percentage depth doses (PDDs) and profiles at various depths were obtained for the 10 cm $\times$ 10 cm open applicator utilising the PTW MP3 therapy beam analyser controlled by the Mephysto mc$^2$ version 2.0 software. The waterproof PTW Pinpoint ionisation chamber (31006) has a measuring volume of 0.015 cm$^3$. The small volume was preferred for the field chamber to minimise errors in the small fields used in this study in the IORT cone cases. The chamber wall comprises 0.56 mm of Poly−Methylmethacrylate ($C_5H_8O_2$) and 0.15 mm of graphite (C) with densities of 1.19 g/cm$^3$ and 0.82 g/cm$^3$, respectively. The chamber has a steel electrode of 0.18 mm in diameter and 4.5 mm in length. The PTW semi-flex chamber (31010) was used as the reference chamber and

placed at the applicator's bottom corner. This chamber has a with a nominal sensitive volume of 0.125 $cm^3$.

The gantry was set to 0° with the beam's central axis directed along the geometrical centre of the water tank. The applicator end was 95 cm from the source with measurements taken at 100 cm source-to-surface distance (SSD) with a 5 cm air gap to the water surface. The Y jaws and MLC symmetric field sizes were set to 19.0 cm each, which is the default field size for the 10 × 10 cm applicator.

The step size used for measuring the PDD curves and the in-plane and cross-plane profiles was 1 mm and 2 mm, respectively. The resulting dose data were smoothed using the three-point algorithm inherent in Mephysto, and the PDD data were converted from ionisation to dose using the IAEA TRS398 stopping power ratios.

In-plane and cross-plane profiles were measured at depths of 1.4 and 2.0 cm for 6 MeV, 2.5, 3.5 and 4.5 cm for 12 MeV, and 2.5, 4.0, 5.0 and 7.0 cm for 18 MeV.

A dose calibration accuracy of 2%/2 mm [32] and overall accuracy of 5%/5 mm have been regarded as being realistic and feasible. Therefore, the relative dose comparison (gamma index or G.I.) criteria for this study have been set as 3%/3 mm.

To further validate the MC dose simulation, applicator factors were verified. These factors are the ratio of the maximum dose on the central axis for a beam of energy E and applicator size X to the maximum dose for the same beam energy, E, with the 10 cm × 10 cm applicator in place. Both measurements are taken at 100 cm SSD with the same amount of monitor units.

The PTW pinpoint ionisation chamber was used to determine the applicator output factor for the 15 cm × 15 cm applicator in water.

#### 2.1.1. BEAMnrc MC simulations

The BEAMnrc MC code was used to model the LINAC using various component modules (CMs). The resulting phase space files obtained from the BEAMnrc simulations were then used as the source in DOSXYZnrc to calculate 3D dose distributions in a voxel-based phantom.

The Siemens Primus LINAC S.N 3606 was used in this study, and in compliance with the Non-Disclosure Agreement, some intimate details of the LINAC have been omitted in this article.

The global electron cutoff energy (ECUT) and photon cutoff energy (PCUT) was set to 0.521 MeV and 0.01 MeV, respectively. The Boundary Crossing Algorithm (BCA) was set to EXACT and the Electron Step algorithm was PRESTA II. Spin effects, Bound Compton scattering, Rayleigh scattering, and atomic relaxations were not implemented.

Phase-space files were scored directly below the end of the 10 cm × 10 cm applicator (z = 95cm) for each beam energy and were used in subsequent DOSXYZnrc simulations. Simulations were repeated for the 15 cm × 15 cm applicator. A schematic of the Siemens Primus Linac can be seen in Figure 1 below.

#### 2.1.2. DOSXYZnrc MC simulations

In DOSXYZnrc, a 20 × 20 × 20 $cm^3$ water tank with voxel dimensions of 0.2 × 0.2 × 0.1 $cm^3$ was constructed, and the XY grid was set to 0.1 × 0.1 $cm^2$ where beam edges were present.

The DOSXYZnrc input parameters were the same as for the BEAMnrc simulations. Enough histories were simulation in BEAMnrc and DOSXYZnrc to obtain a statistical variance below 1% of all MC calculations.

Beam profiles and PDD data were extracted from the resulting DOSXYZnrc data. These were benchmarked against measured data. The energy spectrum for each BEAMnrc electron source was adjusted before re-simulating with the new spectrum based on the G.I. criteria. The process was repeated until suitable comparisons that satisfied the G.I. criteria were achieved. The final energy spectra accepted for the full simulation of the energy set for the 10 cm × 10 cm applicator were used as the BEAMnrc input source for all subsequent simulations (including IORT cones and cutouts) for each of the energies.

MC-calculated output factors were obtained from analysis of $D_{max}$ for the 15 × 15 cm and 10 cm × 10 cm applicators on the beam central axis. The absorbed dose in the voxel at $d_{max}$ for each beam evaluated in this study was obtained. The applicator output factor (15 cm × 15 cm applicator) was determined by relating these doses to the MC-calculated dose at $d_{max}$ for the 10 cm × 10 cm applicator. The measured applicator output factors (OF) were obtained using the PTW pinpoint chamber (31006).

### 2.2. Stage II: dose comparison between water tank measurements and MC simulation for the IORT cones

The Intra-Operative Periscopic Cone system (Radiation Products Design Inc.) model, 1100–00, is the IORT cone system used for this study. A description of the cone system may be found below in Figure 2.

This IORT system may be used on any LINAC by using a coded adapter plate that can slide into the accessory slot of that particular LINAC. The barrel assembly with a periscopic viewer is attached to the adapter plate. The bottom end of the barrel assembly has a hinged door facilitating lateral insertion of the cone into position so that the patient's presence on the treatment couch does not interfere with the cone's insertion process. The cone can slide up to about 20 cm into the periscopic barrel assembly if treatment at shorter SSDs is desired.

There is a spring-loaded movable mirror inside the barrel assembly that may be used to assist in accurately docking the cone whilst viewing the treatment area. The spring mechanism ensures that the mirror is automatically retracted from the field during treatment.

Three Poly-Methyl Methacrylate (PMMA) cones of length 30.5 cm each with inner diameters of 19, 45, and 64mm (defined as the cone set, {C}) were benchmarked in this study. PDDs and profiles were measured for each cone for each energy in the same manner as described for the regular applicator cases in stage I above, with the exception that the PTW semi-flex reference chamber (31010) with a nominal sensitive volume of 0.125 $cm^3$ was placed at the top of the barrel assembly.

PDDs and profiles were also obtained from MC simulations as described above in stage I, but the cones were included in the LINAC model. Comparisons between the measured and MC-produced data was performed in the same manner.

#### 2.2.1. BEAMnrc modelling of the IORT accelerator with open cones

To incorporate the IORT open cones into the LINAC model, the 10 cm × 10 cm applicator, which starts at z = 56 cm, is replaced with three open IORT cones, which start at z = 42cm. The 3.1 mm thick clear PMMA cones utilised in this study had inner diameters corresponding to {C} along their 30.5 cm lengths.

The input source for each of the three energies simulated was the same as that used for the MC simulation for the 10 cm × 10 cm applicator. Each size in {C} replaced the 10 cm × 10 cm applicator. The FLATFILT CM was used to build the cones in BEAMnrc. Each cone consists of 9 layers with varying numbers of conical sections in each layer. The same jaw settings (Y = 19.0 cm and MLC(X) = 19.0 cm) used for the MC simulation for the 10 cm × 10 cm applicator was used for each cone in {C}. The dimensions and material composition of the various components of the cone were obtained from the manufacturer. The top of the barrel assembly has a 1.27 cm lead plate with a circular hole inside it to provide initial collimation of the electrons exiting the treatment head. Each cone consists of a 4.8 mm thick brass plate (with a centre hole with a diameter slightly larger than the inner cone diameter) at the top to collimate the beam to prevent electrons from penetrating the PMMA spacer rings.

For this study, the cone was slid 1 cm into the barrel assembly so that the open end of the cone was at a z distance of 99 cm, resulting in a 1 cm gap between the cone end and the isocentre.

MC simulations were performed for each energy {E} and cone size {C}. Phase-space files were scored at the open end of the cone.

### 2.3. Stage III: manufacturing and measured data of the IORT accelerator with cutouts

The custom-made irregularly shaped cutouts were manufactured with the assistance of the Par-Scientific Block Cutting software and associated hotwire cutter. The indices and outer dimensions of the cutouts for each of the IORT cones in the cone set were sent to the block-cutter. Liquefied Cerrobend (low melting point alloy) was then poured into the 2 cm thick cutout and allowed to cool. Cutouts were then inserted into cones, ensuring the bottom edge of the cutout was precisely level with the open end of the cone.

The identical measurement tools and conditions (described in stage I) were set to acquire the relevant cutout data for the energy set {E} for each IORT cone size in {C}. The water surface was positioned at 100 cm SSD with a 1 cm air gap between the cone end and the water surface. The waterproof PTW Pinpoint ionisation chamber (31006) was used as the field chamber and the PTW semi-flex chamber (31010) was used as the reference chamber and was placed at the corner of the last scraper of the applicator. PDD curves were measured with a 1 mm step size for each energy/cutout combination.

In-plane and cross-plane profiles were measured with 2 mm step size at depths of 1.4 and 2.0 cm for 6 MeV, 2.5 and 4.0 cm for 12 MeV, and 2.5, 4.5, 5.5, and 6.5 cm for 18 MeV. The cutout factor for each combination was analogous to that obtained for the 15 cm × 15 cm applicator in stage I.

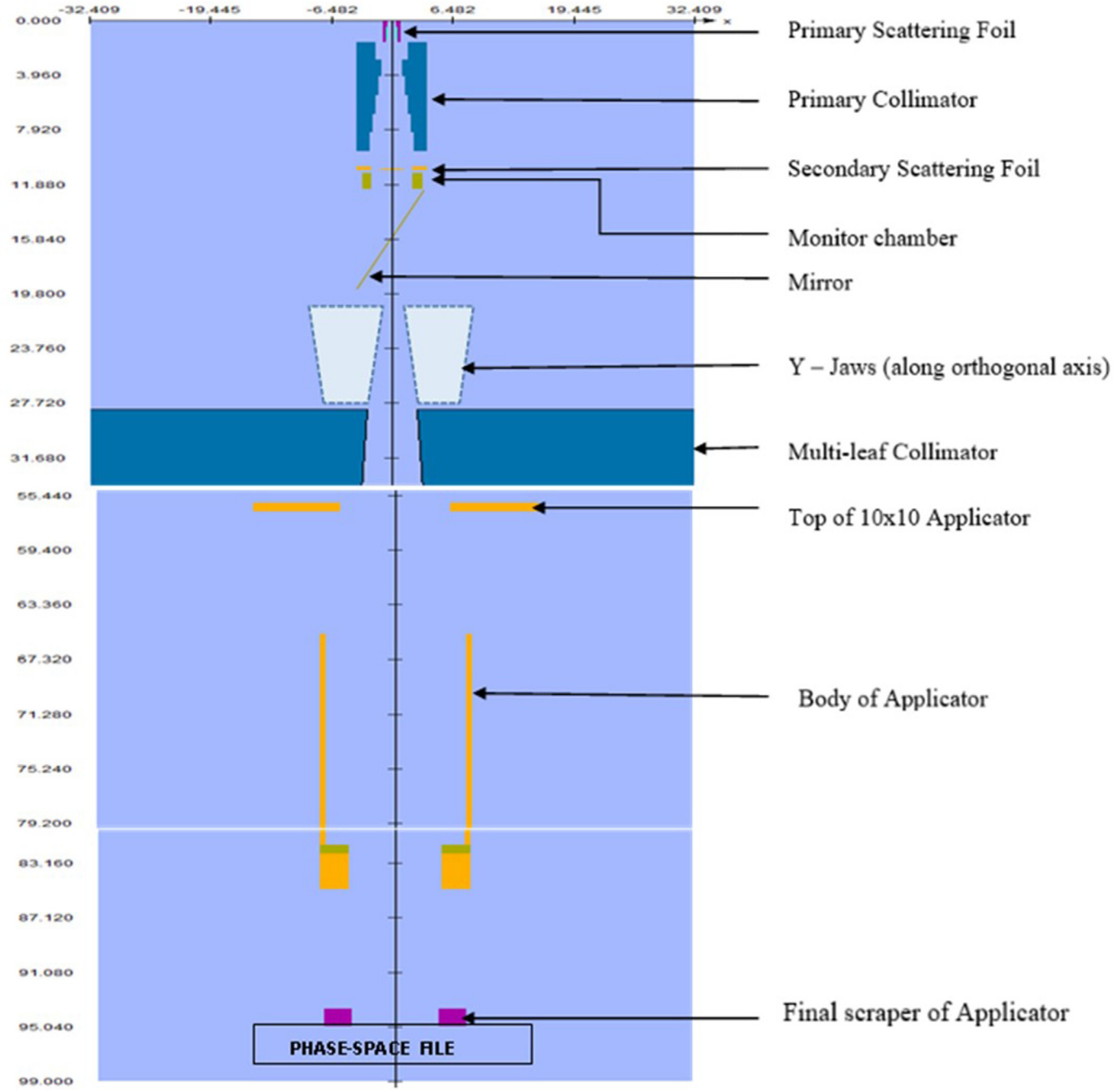


**Figure 1.** The complete Primus LINAC detailing the position of each component of the treatment head together with the 10 cm × 10 cm applicator and phase-space file position.

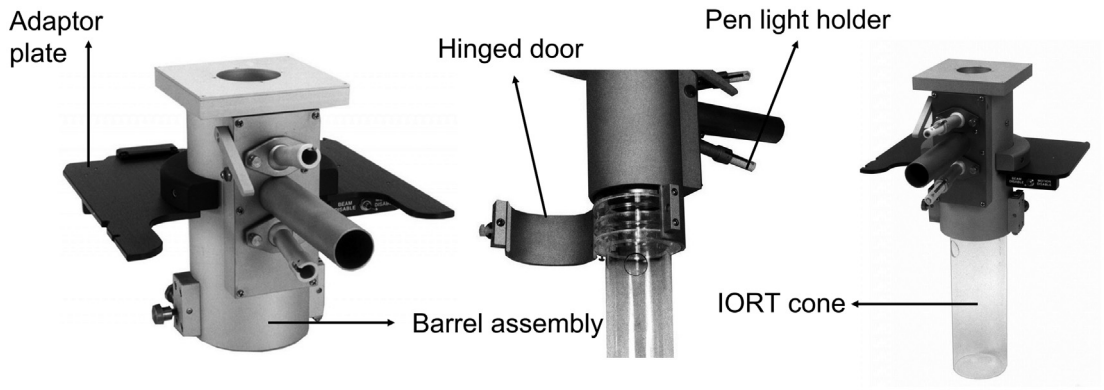


**Figure 2.** The IORT cone system depicts: (a) The adaptor plate and barrel assembly. (b) The hinged door for lateral docking of the cone and penlight holder for viewing the treatment site (c) the fully assembled cone system (Courtesy of Radiation Products Inc.).

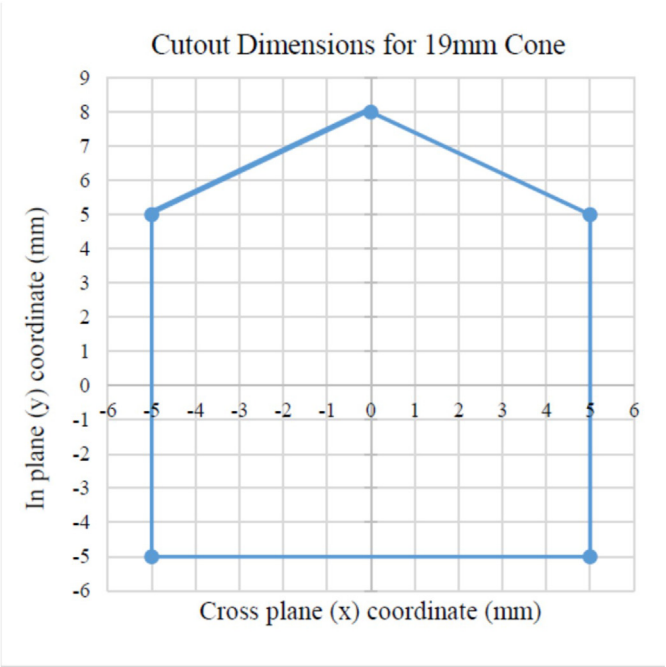


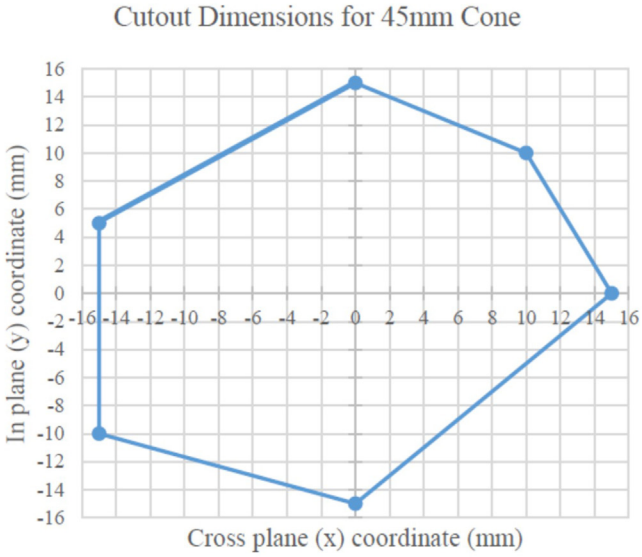


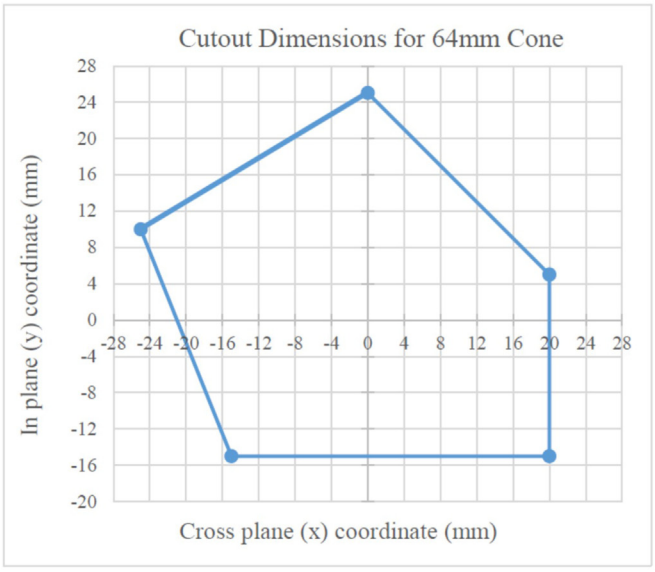


**Figure 3.** Coordinates for block cutouts used in manufacturing and BEAMnrc simulations for the cone sizes used in this study.

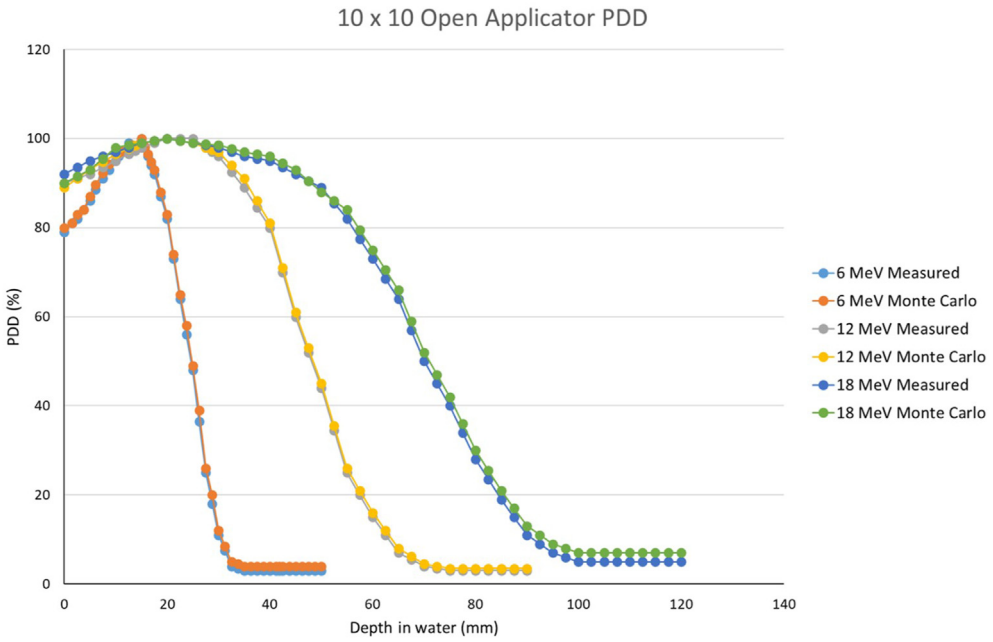


**Figure 4.** Comparison of measured and MC PDDs for the energy set {E} with 10 cm × 10 cm applicator: Data corresponds within 3%/3 mm in over 99 % of the comparison data points. Uncertainty in the MC data is within 1%.

**Table 1.** Shows the component modules (CMs) used in BEAMnrc for the LINAC simulation.

| Component | CM | Material | ECUT | PCUT |
|---|---|---|---|---|
| Primary Scattering Foil | FLATFILT | combinations of brass, lead alloy, and gold | 0.521MeV | 0.01MeV |
| Primary Collimator | FLATFILT | tungsten | 0.521MeV | 0.01MeV |
| Secondary Scattering Foil | FLATFILT | aluminium and Kapton | 0.521MeV | 0.01MeV |
| Chamber | CHAMBER | gold and Kapton | 0.521MeV | 0.01MeV |
| Mirror | MIRROR | - | 0.521MeV | 0.01MeV |
| XY collimators | JAWS | tungsten | 0.521MeV | 0.01MeV |
| Multi-leaf Collimator | MLC | tungsten | 0.521MeV | 0.01MeV |
| Applicator | APPLICAT | aluminium, stainless steel and brass | 0.521MeV | 0.01MeV |

The BEAMnrc electron source was a parallel circular beam of 0.1 cm diameter located just above the first component of the accelerator head (the primary scattering foil, Table 1). Its input energy spectrum was poly-energetic. The energy spectra describing the electron sources for {E} had 5 energy bins, each with varying relative intensities. The energy bins ranged from 6.75 to 8.5 MeV for the 6 MeV source, 11.2–16.4 MeV for the 12 MeV source and 17.2–23.5 MeV for the 18 MeV source.

### *2.3.1. BEAMnrc modelling of the IORT accelerator with cutouts*

The simulation sources and geometry were the same as those reported in stages I and II. The FLATFILT CM was again used to build the cones and cutouts in BEAMnrc. As previously mentioned, the cones consisted of 9 layers with conical sections in each layer. For these cases, the cones end at 97 cm, allowing room for the added cutout into the last 2 cm of each cone.

The cutout was modelled by the BLOCK CM available in BEAMnrc. Modelling the cutout required input of the z distance of the front (97 cm) and back (99 cm) of the cutout. The outer boundaries of each block were circular and equivalent to the inner diameter of each cone. In order to model this in BEAMnrc, the size of the outer rectangular boundaries of the CM were chosen to be equal to the radius the cone being used. In a previous study [42], it was suggested that only a 1 mm of Cerrobend be used around the aperture to improve the efficiency of the MC calculations for 6–12 MeV beams. The thickness of the Cerrobend increases to 25 mm for 20 MeV. Therefore, for this study, it is safe to assume that any particles striking the additional Cerrobend that exists off-axis beyond 1 mm would have been effectively stopped by the initial 1 mm of Cerrobend for the lower energies. Accurate input of the cutout geometry was accomplished by entering the x and y coordinates of the indices (Figure 3) of each defining point of the cutout.

**Table 2.** Absolute differences between measured and MC-calculated characteristic points on the PDD curve for the beam set's 10 × 10 cm applicator.

| | 6MeV | | | 12MeV | | | 18MeV | | |
|---|---|---|---|---|---|---|---|---|---|
| | Meas | MC | Diff | Meas | MC | Diff | Meas | MC | Diff |
| $D_S$ (%) | 79.6 | 78.7 | **-0.9** | 91.0 | 88.7 | **-2.3** | 95.4 | 90.2 | **-5.2** |
| $R_{max}$ (cm) | 1.32 | 1.35 | **0.03** | 2.28 | 2.35 | **0.07** | 1.40 | 1.45 | **0.05** |
| $R_{90}$ (cm) | 1.82 | 1.78 | **-0.04** | 3.47 | 3.55 | **0.08** | 4.72 | 4.75 | **0.03** |
| $R_{80}$ (cm) | 2.02 | 2.01 | **-0.01** | 3.94 | 3.95 | **0.01** | 5.65 | 5.70 | **0.05** |
| $R_{50}$ (cm) | 2.44 | 2.44 | **0.00** | 4.86 | 4.87 | **0.01** | 7.14 | 7.20 | **0.06** |

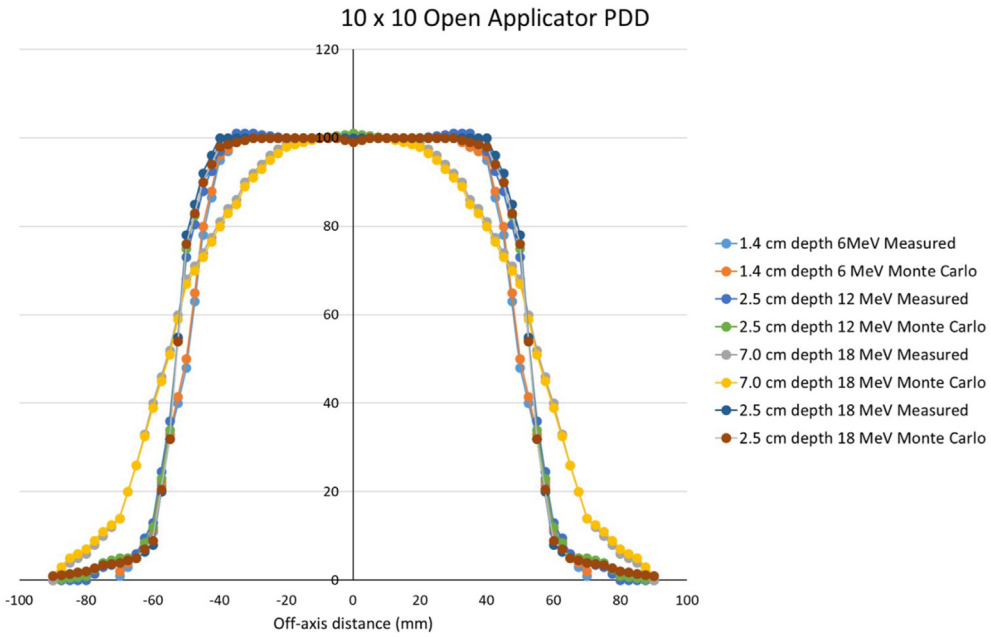


**Figure 5.** Comparison of measured and MC profiles at 1.4 cm depth, 6 MeV, 2.5 cm depth, 12 MeV, 7.0 and 2.5 cm depth 18 MeV for the 10 × 10 cm applicator. Data corresponds within 3%/3 mm. Uncertainty in the MC data is within 1%.

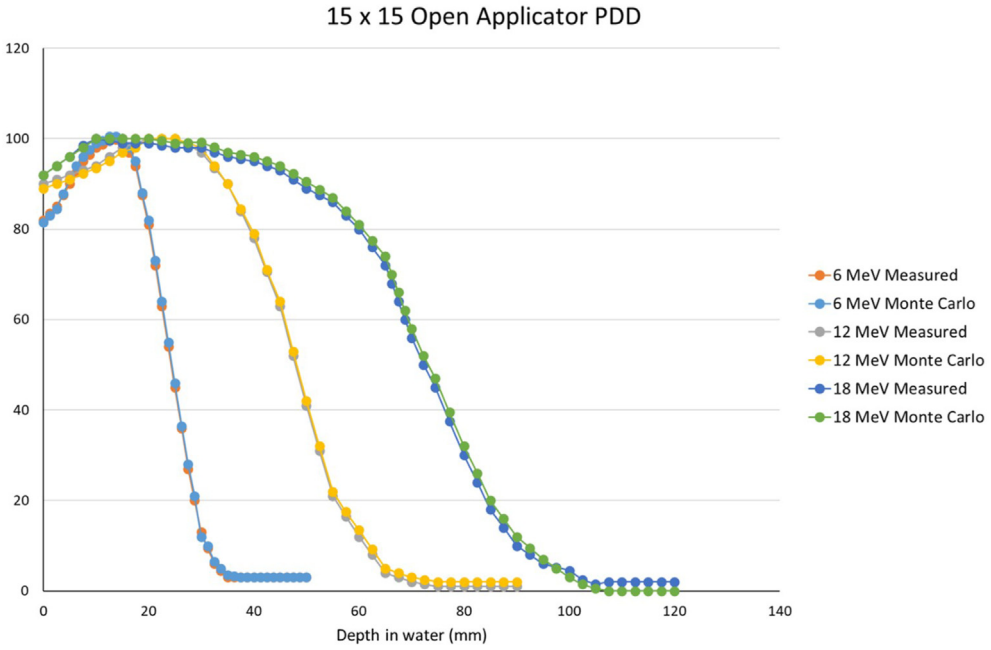


**Figure 6.** Comparison of measured and MC PDDs for {E} and the 15 cm × 15 cm applicator. Uncertainty in the MC data is within 1%.

**Table 3.** Absolute differences between measured and MC-calculated characteristic points on the PDD curve for the 15 cm × 15 cm applicator for {E}.

| | 6MeV | | | 12MeV | | | 18MeV | | |
|---|---|---|---|---|---|---|---|---|---|
| | Meas | MC | Diff | Meas | MC | Diff | Meas | MC | Diff |
| **$D_s$ (%)** | 83.3 | 82.1 | **-1.2** | 91.3 | 88.5 | **-2.8** | 94.5 | 92.9 | **-1.6** |
| **$R_{max}$ (cm)** | 1.20 | 1.22 | **0.02** | 2.10 | 2.14 | **0.04** | 1.60 | 1.67 | **0.07** |
| **$R_{90}$ (cm)** | 1.82 | 1.79 | **-0.03** | 3.59 | 3.49 | **-0.10** | 4.98 | 5.16 | **0.18** |
| **$R_{80}$ (cm)** | 2.02 | 1.99 | **-0.03** | 4.02 | 3.94 | **-0.08** | 5.90 | 6.04 | **0.14** |
| **$R_{50}$ (cm)** | 2.46 | 2.42 | **-0.04** | 4.89 | 4.82 | **-0.07** | 7.30 | 7.42 | **0.12** |

**Table 4.** Comparison of measured and MC-calculated output factors (OF) for the 15 cm × 15 cm applicator for the beam set.

| | 6MeV | | | 12MeV | | | 18MeV | | |
|---|---|---|---|---|---|---|---|---|---|
| | Meas | MC | %Diff | Meas | MC | %Diff | Meas | MC | %Diff |
| **15 × 15cm** | 1.024 | 1.018 | -0.59 | 0.994 | 0.987 | -0.70 | 0.984 | 0.979 | -0.51 |

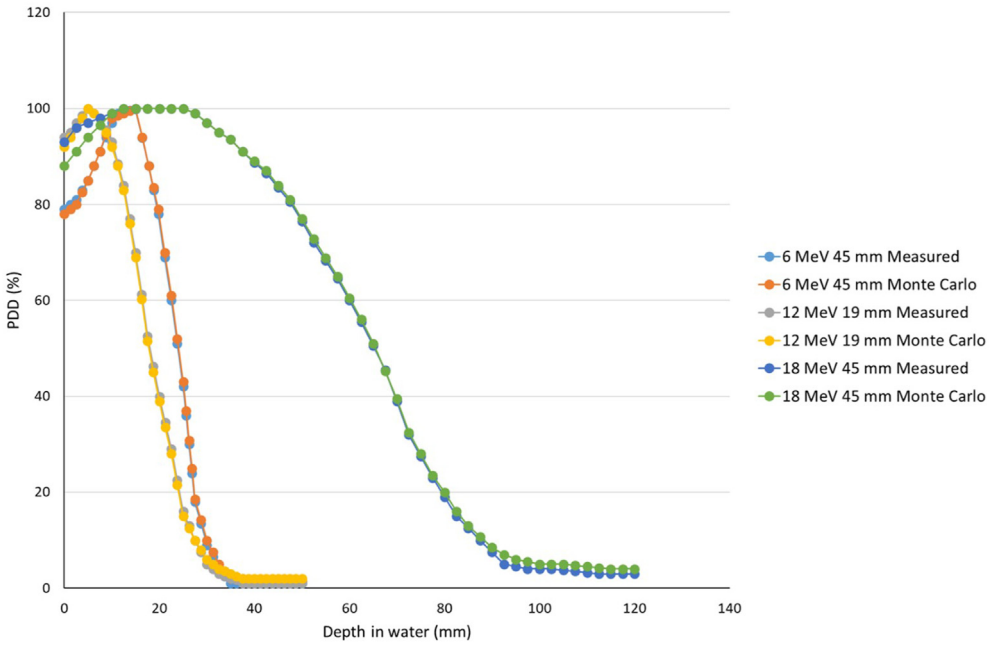


**Figure 7.** Comparison of measured and MC PDDs for the 45 mm cone at 6 MeV, the 19 mm cone at 12 MeV, and the 45 mm cone at 18 MeV. Uncertainty in the MC data is within 1%.

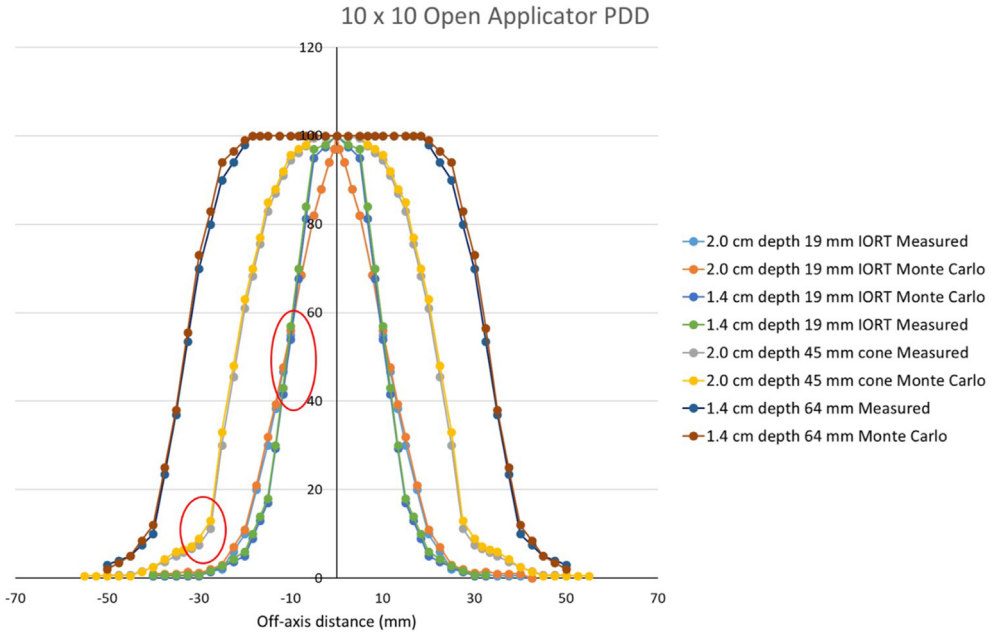


**Figure 8.** Comparison of measured and MC profiles for 6 MeV 2.0 cm depth, 1.4 cm depth for the 19 mm IORT Open Cone, and 1.4 cm for the depth 64 mm cone, and at 2.0 cm depth for the 45 mm cone. The encircled regions indicate where the 3%/3 mm criteria were exceeded. Uncertainty in the MC data is within 1%.

## 3. Results

### 3.1. Monte Carlo commissioning of the LINAC

The first stage in this study involved setting up an accurate BEAMnrc model of the Siemens Primus. Dosimetric data was obtained for the 10 cm × 10 cm and 15 cm × 15 cm applicators.

In Figure 4, PDD data is compared between the beam with energy set {E} obtained from water tank measurements and BEAMnrc simulations for the 10 cm × 10 cm applicator. Table 2 below shows the absolute differences of pertinent characteristic MC-calculated points relative to measurements for these PDD curves. Differences are observed at the surface where the dose ($D_s$) deviates by 5.2 % between the measured and BEAMnrc data. The rest of the dosimetric parameters, namely the range for maximum dose ($R_{max}$), $R_{90}$, $R_{80}$ and $R_{50}$, shows good agreement between the data sets. All simulation data has an uncertainty within 1%.

Figure 5 shows in-plane beam profiles. We can see good agreement between the measured and BEAMnrc data at depths of 7.0 and 2.5 cm, respectively, for 18 MeV.

Figure 6 shows the measured and BEAMnrc generated PDD data for {E} for the 15 cm × 15 cm applicator.

Table 3 below shows the absolute differences of pertinent characteristic MC-calculated points relative to measurements for PDD curves for {E} for the 15 cm × 15 cm applicator.

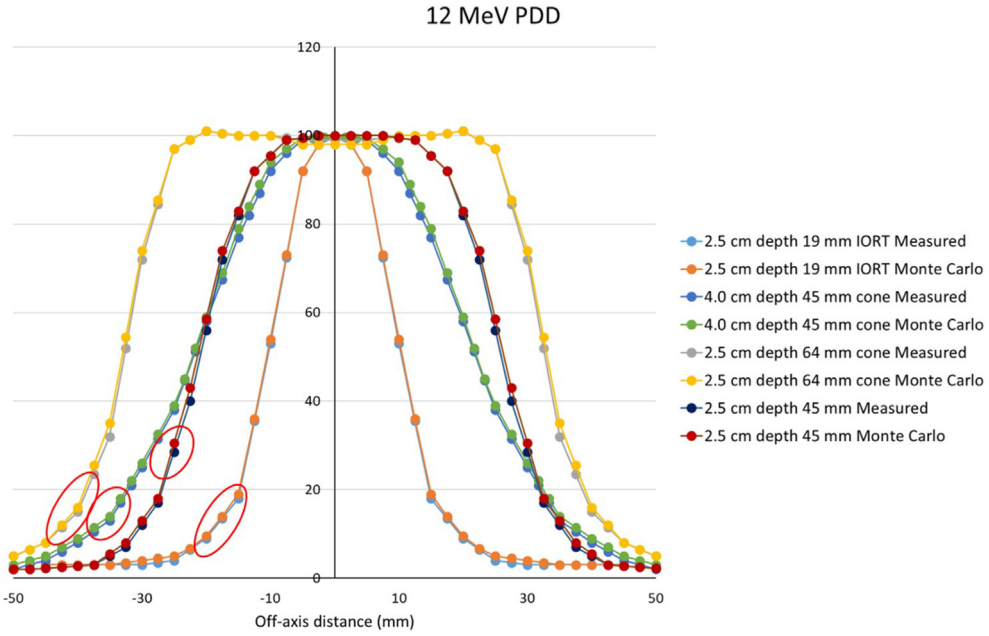


**Figure 9.** Comparison of measured and MC profiles for 12 MeV at 2.5 cm depth for the 19 mm IORT Open Cone, and 2.5 cm depth for the 45 mm cone, 4 cm depth for the 45 mm cone, and at 2.5 cm depth for the 64 mm cone. The encircled regions indicate where the 3%/3 mm criteria were exceeded. Uncertainty in the MC data is within 1%.

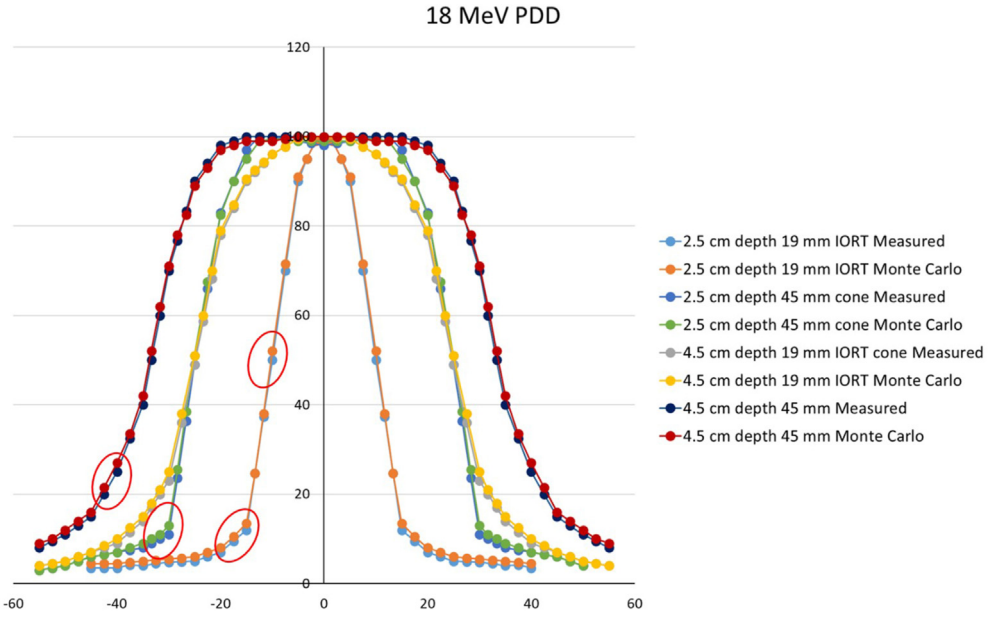


**Figure 10.** Comparison of measured and MC profiles for 18 MeV at 2.5 cm depth, and 4.5 cm depth for the 19 mm IORT Open Cone, and 2.5 cm depth, and at 4.5 cm depth for the 45 mm cone. The encircled regions indicate where the 3%/3 mm criteria were exceeded. Uncertainty in the MC data is within 1%.

A direct comparison of the depths $R_{max}$, $R_{90}$, $R_{80}$, and $R_{50}$ (Table 3) showed an increase in absolute differences with increased energy. The largest difference was for $R_{90}$ for the 18 MeV beam, with a difference of 1.8 mm. The maximum difference in surface dose was for the 12 MeV beam, with the calculated value being 2.8% lower than the measurement. The BEAMnrc surface doses ($D_s$) were lower than the measurement for all energies. Output factors were also calculated between the three beam energies studied for the 15 cm × 15 cm applicator. Results are shown in Table 4. Very good agreement is shown between measured and simulated data (MC) with differences within one percent.

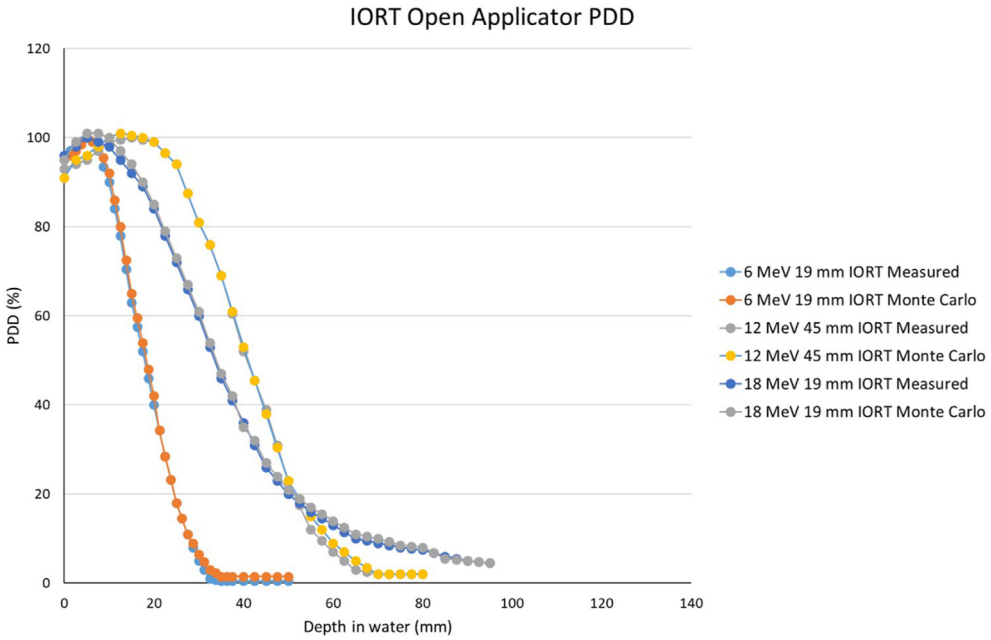


**Figure 11.** PDD data for IORT cones with cutouts for the 19 mm cone and for 6 and 18 MeV, and for the 45 mm cone for 12 MeV. Uncertainty in the MC data is within 1%.

**Table 5.** Absolute differences between measured and MC-calculated characteristic points on the PDD curve for the 19mm IORT Open cone for {E}.

| | 6MeV | | | 12MeV | | | 18MeV | | |
|---|---|---|---|---|---|---|---|---|---|
| | Meas | MC | Diff | Meas | MC | Diff | Meas | MC | Diff |
| $D_S$ (%) | 95.1 | 90.7 | **-4.4** | 93.7 | 92.3 | **-1.4** | 94.9 | 92.2 | **-2.7** |
| $R_{max}$ (cm) | 0.60 | 0.75 | **0.15** | 1.20 | 1.15 | **-0.05** | 1.35 | 0.95 | **0.40** |
| $R_{90}$ (cm) | 1.19 | 1.33 | **0.14** | 2.21 | 2.10 | **-0.11** | 2.70 | 2.64 | **0.06** |
| $R_{80}$ (cm) | 1.48 | 1.58 | **0.10** | 2.60 | 2.48 | **-0.12** | 3.28 | 3.17 | **0.11** |
| $R_{50}$ (cm) | 2.05 | 2.13 | **0.08** | 3.50 | 3.44 | **-0.06** | 4.53 | 4.51 | **0.02** |

**Table 6.** Absolute differences between measured and MC-calculated characteristic points on the PDD curve for the 45mm IORT Open cone for {E}.

| | 6MeV | | | 12MeV | | | 18MeV | | |
|---|---|---|---|---|---|---|---|---|---|
| | Meas | MC | Diff | Meas | MC | Diff | Meas | MC | Diff |
| $D_S$ (%) | 78.6 | 76.5 | **-2.1** | 90.6 | 87.6 | **-2.4** | 93.9 | 88.3 | **-5.6** |
| $R_{max}$ (cm) | 1.20 | 1.25 | **0.05** | 2.10 | 1.95 | **-0.15** | 1.95 | 2.05 | **0.10** |
| $R_{90}$ (cm) | 1.81 | 1.77 | **-0.04** | 3.31 | 3.34 | **0.03** | 4.32 | 4.25 | **-0.07** |
| $R_{80}$ (cm) | 1.99 | 1.93 | **-0.06** | 3.78 | 3.75 | **-0.03** | 5.02 | 4.94 | **-0.08** |
| $R_{50}$ (cm) | 2.39 | 2.37 | **-0.02** | 4.65 | 4.66 | **0.01** | 6.60 | 6.47 | **-0.13** |

**Table 7.** Absolute differences between measured and MC-calculated characteristic points on the PDD curve for the 64mm IORT Open cone for {E}.

| | 6MeV | | | 12MeV | | | 18MeV | | |
|---|---|---|---|---|---|---|---|---|---|
| | Meas | MC | Diff | Meas | MC | Diff | Meas | MC | Diff |
| **$D_s$ (%)** | 78.0 | 77.1 | **-0.9** | 84.6 | 87.2 | **2.6** | 95.1 | 93.5 | **-1.6** |
| **$R_{max}$ (cm)** | 1.30 | 1.35 | **0.05** | 2.60 | 2.45 | **-0.15** | 1.80 | 0.95 | **-0.95** |
| **$R_{90}$ (cm)** | 1.75 | 1.77 | **0.02** | 3.71 | 3.46 | **-0.25** | 4.50 | 4.36 | **-0.14** |
| **$R_{80}$ (cm)** | 1.95 | 1.97 | **0.02** | 4.08 | 3.90 | **-0.18** | 5.38 | 5.30 | **-0.08** |
| **$R_{50}$ (cm)** | 2.37 | 2.38 | **0.01** | 4.83 | 4.81 | **-0.02** | 6.87 | 6.85 | **-0.02** |

### 3.2. Comparison of mc simulations and measurements with iort open cones

All the PDD curves and profiles for all energies were measured with the same resolution as the MC data points. Figure 7 shows PDD data for the cones and beam energies used in this study.

Table 5, 6 and 7 show the absolute differences of pertinent characteristic MC- calculated points relative to measurements for the cone set {C} respectively for 6, 12, and 18 MeV PDD curves.

Comparing the measured in-plane and cross-plane profiles with the MC simulation data yielded similar results. Only the cross-plane results are reported below in Figure 8 for 6 MeV electron beams. Similar data are also shown for the 12 and 18 MeV beam cases in Figures 9 and 10.

### 3.3. Cone Factors

The cone factors (C.F.) for the IORT open cones were measured analogously to the applicator output factor determination. The PTW pinpoint ionisation chamber was used to measure ionisation at $z_{max}$, which varies with field size and energy for each cone [43]. The ionisation measurements obtained were corrected for the variation with depth of the water-to-air stopping power ratios, $sw_{,air}$.

The MC-calculated cone factors were obtained by analysing the 3-D dose distribution on the beam central axis for each of the cones and energy and relating the doses at the respective $d_{max}$ depths for the cone applicator relative to the 10 cm × 10 cm applicator. A comparison between the measured and MC-calculated cone factors for {C} appear in Table 8 below. Uncertainty in the MC data is within 1%.

### 3.3. Comparison of mc simulations and measurements for iort cones with irregularly shaped cutouts

Figure 11 shows PDD data for IORT cones with cutouts inserted, as depicted in Figure 3. Data are shown for the 19 mm cone with cutout (top left) and (top right) for the 6 and 18 MeV cases. The 45 mm cone data is shown in the bottom left and right panels for the 12 and 18 MeV cases. Good agreement is demonstrated between the measured and simulated PDD data showing that the BEAMnrc model is accurate. Tables 9, 10, and 11 show the data difference for the dosimetric beam parameters used throughout this study. All differences were within 3% of the local values. In Figure 12, beam profile data are shown for the 19 mm cone for 6 (left) and 18 MeV (right) beam energy. All simulation data has an uncertainty within 1%.

**Table 8.** Comparison between the measured and MC-calculated cone factors (C.F.) for {C} over energies contained in {E}.

| | 6MeV | | | 12MeV | | | 18MeV | | |
|---|---|---|---|---|---|---|---|---|---|
| | Meas | MC | % diff | Meas | MC | % diff | Meas | MC | % diff |
| **19mm Cone** | 0.431 | 0.463 | 7.42 | 0.845 | 0.912 | 7.93 | 1.054 | 1.115 | 5.82 |
| **45mm Cone** | 1.043 | 1.059 | 1.53 | 1.204 | 1.181 | -1.92 | 1.232 | 1.211 | -1.71 |
| **64mm Cone** | 1.114 | 1.121 | 0.63 | 1.232 | 1.222 | -0.85 | 1.234 | 1.226 | -0.64 |

**Table 9.** Absolute differences between measured and MC-calculated characteristic points on the PDD curve for the 19 mm IORT cutout for {E}.

| | 6MeV | | | 12MeV | | | 18MeV | | |
|---|---|---|---|---|---|---|---|---|---|
| | Meas | MC | Diff | Meas | MC | Diff | Meas | MC | Diff |
| **$D_s$ (%)** | 95.4 | 95.1 | **-0.3** | 98.2 | 95.9 | **-2.3** | 94.9 | 95.5 | **0.6** |
| **$R_{max}$ (cm)** | 0.50 | 0.45 | **-0.05** | 0.25 | 0.45 | **0.20** | 1.35 | 0.55 | **0.20** |
| **$R_{90}$ (cm)** | 0.97 | 0.98 | **0.01** | 1.25 | 1.27 | **0.02** | 1.64 | 1.68 | **0.02** |
| **$R_{80}$ (cm)** | 1.20 | 1.20 | **0.00** | 1.63 | 1.64 | **0.01** | 2.09 | 2.16 | **0.07** |
| **$R_{50}$ (cm)** | 1.75 | 1.74 | **-0.01** | 2.49 | 2.53 | **0.04** | 3.28 | 3.32 | **0.04** |

**Table 10.** Absolute differences between measured and MC-calculated characteristic points on the PDD curve for the 45 mm IORT cutout for {E}.

| | 6MeV | | | 12MeV | | | 18MeV | | |
|---|---|---|---|---|---|---|---|---|---|
| | Meas | MC | Diff | Meas | MC | Diff | Meas | MC | Diff |
| **$D_s$ (%)** | 85.3 | 86.7 | **1.4** | 93.4 | 91.6 | **-1.8** | 98.4 | 96.2 | **-2.2** |
| **$R_{max}$ (cm)** | 1.10 | 1.05 | **-0.10** | 1.50 | 1.25 | **-0.25** | 0.95 | 1.15 | **0.20** |
| **$R_{90}$ (cm)** | 1.67 | 1.62 | **-0.05** | 2.61 | 2.53 | **-0.12** | 3.00 | 3.00 | **0.00** |
| **$R_{80}$ (cm)** | 1.89 | 1.82 | **-0.07** | 3.04 | 2.96 | **-0.08** | 3.73 | 3.75 | **0.02** |
| **$R_{50}$ (cm)** | 2.37 | 2.33 | **-0.04** | 4.07 | 4.03 | **-0.04** | 5.23 | 5.24 | **0.01** |

**Table 11.** Absolute differences between measured and MC-calculated characteristic points on the PDD curve for the 64 mm IORT cutout for {E}.

| | 6MeV | | | 12MeV | | | 18MeV | | |
|---|---|---|---|---|---|---|---|---|---|
| | Meas | MC | Diff | Meas | MC | Diff | Meas | MC | Diff |
| **$D_s$ (%)** | 84.3 | 82.2 | **-2.1** | 96.3 | 93.0 | **-3.3** | 98.3 | 96.1 | **-2.2** |
| **$R_{max}$ (cm)** | 1.25 | 1.25 | **0.00** | 1.50 | 1.65 | **0.15** | 0.90 | 0.65 | **-0.35** |
| **$R_{90}$ (cm)** | 1.76 | 1.74 | **-0.02** | 2.95 | 2.92 | **-0.03** | 3.45 | 3.46 | **0.01** |
| **$R_{80}$ (cm)** | 1.96 | 1.93 | **-0.03** | 3.45 | 3.40 | **-0.05** | 4.35 | 4.33 | **-0.02** |
| **$R_{50}$ (cm)** | 2.39 | 2.37 | **-0.02** | 4.50 | 4.45 | **-0.05** | 6.06 | 6.03 | **-0.03** |

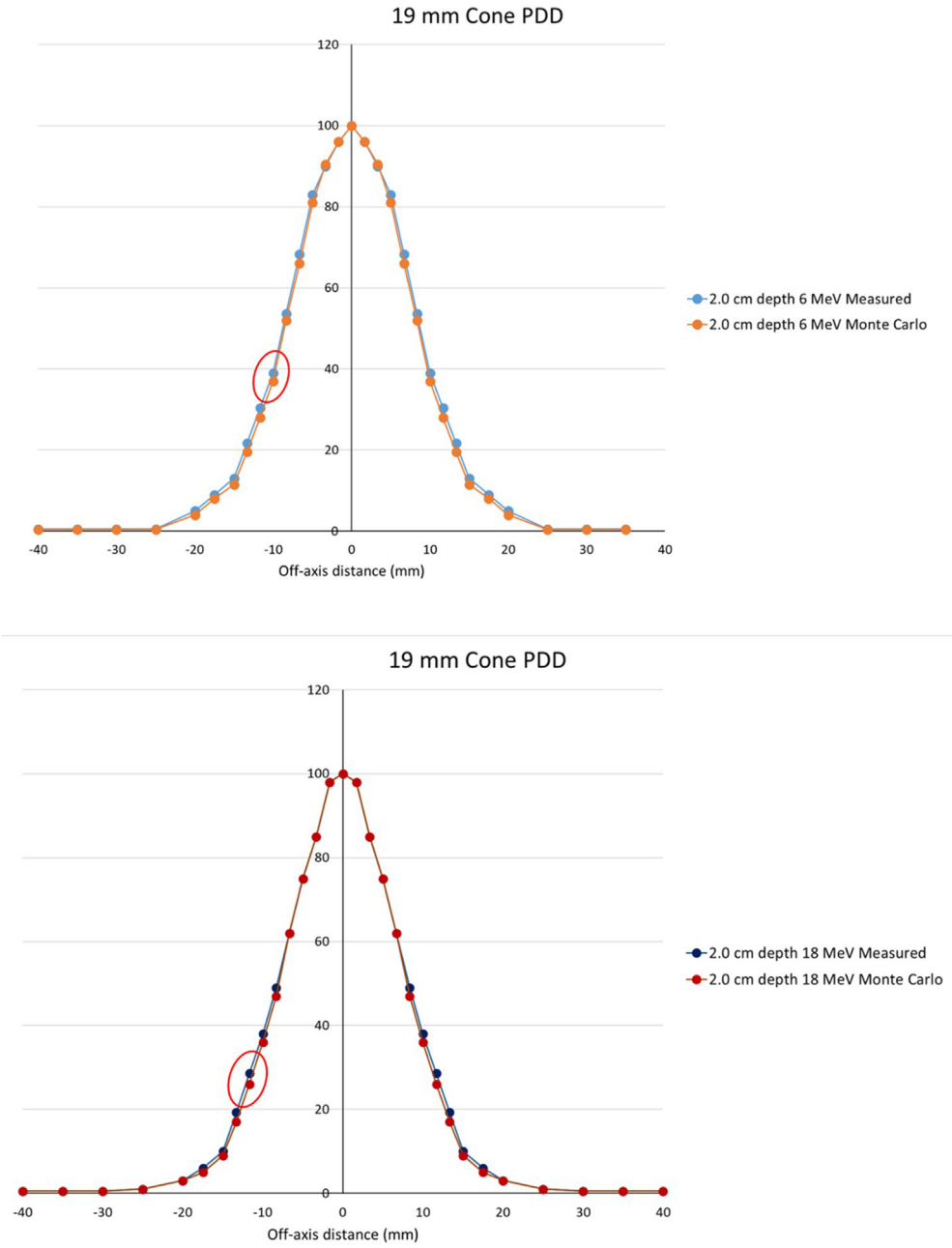


**Figure 12.** Profile data for the 6 and 18 MeV electron beams for the 19 mm cone. The encircled regions indicate where the 3%/3 mm criteria were exceeded. Uncertainty in the MC data is within 1%.

## 4. discussion

The purpose of this study was to perform Monte Carlo commissioning of the Siemens Primus LINAC for 6, 12, and 18 MeV electron beams. The electron beam sources could be used in benchmarking dosimetric parameters for beams collimated by IORT cones with and without custom made cutouts against water tank measurements. The commissioning process involves benchmarking MC-calculated beam data against measurements, using acceptance criteria based on clinically accepted beam data tolerances.

The first step was to model the LINAC in BEAMnrc by using detailed descriptions of each treatment head component supplied by the vendor. Phase space files produced by BEAMnrc were used as respective input sources for DOSXYZnrc. This MC simulation code produced 3-D dose distributions from which the relevant PDD and profiles were obtained for comparison with measured data.

The main results for this process (Stage I, section 3.1) are shown in Figures 4, 5, and 6. The PDD and profile data show that it replicates water tank data within 3%/3 mm in almost all cases. The surface dose ($D_s$) in Table 2 shows a discrepancy of 5.2 % with the rest of the beam parameter data, namely $R_{max}$, $R_{90}$, $R_{80}$ and $R_{50,}$ falling well within the above criteria. One might ask why such criteria for 3 %/3 mm? The ultimate goal is to use MC simulation to guide the dosimetry of exposed tumours in IORT and FLASH-IORT procedures, especially when custom-made cutouts are involved for final electron beam collimation. Here the tumour position is known, and the beam can be directed on the visible tumour volume.

Unacceptable comparisons (larger than the criteria above) would imply the need to further investigate the accuracy and validity of the measurements. To ensure the MC modelling process is accurate, great care should be taken to ensure that the CMs and input parameters used in the MC build of the accelerator are correct. The incident electron energy

(source) has been found to be the primary tuning parameter for electron beam simulations. Chetty et al. found that a 0.2 MeV change in electron energy results in a one mm change in beam range [30]. The electron source contained an energy spectrum tuned to produce acceptable PDD and profile comparisons for this study.

Table 3 shows that measured and MC generated beam dose parameters were within the G.I. criteria set for this study with larger discrepancies for $\mathbf{D_s}$ at 12 and 18 MeV.

In Table 4, the differences in calculated and measured applicator factors were within 0.7%, implying that the MC-model of the LINAC can accurately simulate scattering conditions to produce an output factor that is confirmed with measurements.

For IORT cone dose commissioning, only the 10 × 10 and 15 cm × 15 cm applicators were considered, mainly to determine the correct energy distribution for the electron sources of the three energies. Since cone diameters were well within the 10 cm × 10 cm field size (largest being 64 mm diameter), the commissioning for this applicator field size proved to be adequate. This was shown in the results discussed below.

In stage II (section 3.2), the tuned electron sources were used to produce PDD and profile data for IORT cone-collimated electron beams for 6, 12, and 18 MeV Figure 7 shows good agreement with PDD data for MC benchmarked against measurements. In Figures 8, 9, and 10, the encircled areas indicated points lying outside the criteria set above. These points are mainly on the steep beam edges or in the outer regions of the penumbra. The majority of the dose profile data was within the criteria. This is further stipulated in the dosimetric parameter comparison in Tables 5, 6, and 7 for the 6, 12, and 18 MeV beams, respectively. The only significant discrepancy was in the surface dose ($D_s$). In Tables 5 and 7, $R_{max}$ posed differences outside the criteria for the 19- and 64-mm cones at 18 MeV. The values were 0.4 and 0.95 cm, respectively. The $R_{90}$ and $R_{80}$ values fell within the criteria, which is dosimetrically more important since it determines the tumour thickness that can be treated at these energies and cone sizes.

In Table 8, cone factors differ by more than 3 % for the 19 mm cone at all three beam energies, varying between 6 and 9 %. A factor that can influence this is the uncertainty in the output measurement at the small cone openings since the chamber will measure an average signal due to the local dose gradient in the 19 mm cone (see Figure 8, top left panel as an example). The measured data is always lower than the MC data since the MC water tank has a higher resolution, minimising the averaging effect compared to the finite-sized ionisation chamber. This effect is not present at the larger cone sizes due to a uniform dose region in the neighbourhood of the beam central axis.

In section 3, the results are shown for the IORT cones with custom made inserts of irregular shapes. Since we are dealing with irregular shapes, the MC method for dose calculation would, in this case, be the most suitable approach. This step could only be reached after stage I and stage II of this study to commission the MC results with measurement. Since we continue with verification in stage III, we limit the benchmark data to field PDD and profile data, as shown in Figures 11 and 12 Here we see good agreement with the MC and water tank measured data. This is reflected in the dosimetric data in Tables 9, 10, and 11 for the three cone sizes in {C} at the beam energies {E} studied. Here we see that all electron PDD range data are within 0.2 cm. Irregularly shaped cutouts create complexities that can be handled in MC simulation and may alter PDD profiles due to uneven lateral electron build-up towards the beam axis.

## 5. Conclusion

This study demonstrated that MC simulation could replicate electron beams within a criterion of 3%/3 mm by first commissioning it against regular applicator collimated electrons. Then, the derived electron sources are used in subsequent simulations when IORT open cones are used without and with irregularly shaped electron cutouts. These results also apply to FLASH-IORT using electron beams and high dose rates.

Validation was verified through measurements in a water tank for 6, 12 and 18 MeV electron beams, with 19-, 45-, and 64-mm apertures cone sizes. The only problem is the accuracy of cone factors for the 19 mm cone size. However, it can be attributed to the local dose gradient in the beam profile and the finite size of the ionisation chamber.

## Declarations

### *Author contribution statement*

G.L. Lazarus: Conceived and designed the experiments; Performed the experiments; Analyzed and interpreted the data; Contributed reagents, materials, analysis tools or data; Wrote the paper.

D. van Eeden: Analyzed and interpreted the data; Contributed reagents, materials, analysis tools or data; Wrote the paper.

F.C.P. du Plessis: Conceived and designed the experiments; Analyzed and interpreted the data; Wrote the paper.

### *Funding statement*

This research did not receive any specific grant from funding agencies in the public, commercial, or not-for-profit sectors.

### *Data availability statement*

Data included in article/supp. material/referenced in article.

### *Declaration of interest's statement*

The authors declare no conflict of interest.

### *Additional information*

No additional information is available for this paper.

## References

[1] R. Benson, S. Mallick, Therapeutic index and its clinical significance, Pract. Radiat. Oncol (November 2020) 191–192.

[2] J.D. Zindler, C.R. Thomas, S.M. Hahn, A.L. Hoffmann, E.G.C. Troost, P. Lambin, Increasing the therapeutic ratio of stereotactic ablative radiotherapy by individualized isotoxic dose prescription, JNCI J. Natl. Cancer Inst. (2) (2016) 108.

[3] A. Pilar, M. Gupta, S.G. Laskar, S. Laskar, Intraoperative radiotherapy: review of techniques and results, Ecancermedicalscience (2017 Jun 29) 11.

[4] F.A. Holman, M.G. Haddock, L.L. Gunderson, M. Kusters, G.A.P. Nieuwenhuijzen, H.A. van den Berg, et al., Results of intraoperative electron beam radiotherapy containing multimodality treatment for locally unresectable T4 rectal cancer: a pooled analysis of the Mayo Clinic Rochester and Catharina Hospital Eindhoven, J. Gastrointest. Oncol. 7 (6) (2016) 903–916.

[5] F. Roeder, B. Lehner, L. Saleh-Ebrahimi, F.W. Hensley, A. Ulrich, I. Alldinger, et al., Intraoperative electron radiation therapy combined with external beam radiation therapy and limb sparing surgery in extremity soft tissue sarcoma: a retrospective single center analysis of 183 cases, Radiother. Oncol. [Internet] 119 (1) (2016 Apr 1) 22–29. http://www.thegreenjournal.com/article/S0167814015006192/fulltext.

[6] T. Conroy, J.B. Bachet, A. Ayav, F. Huguet, A. Lambert, C. Caramella, et al., Current standards and new innovative approaches for treatment of pancreatic cancer, Eur. J. Cancer [Internet] 57 (2016 Apr 1) 10–22. http://www.ejcancer.com/article/S0959804916000022/fulltext.

[7] G. Fastner, C. Gaisberger, J. Kaiser, P. Scherer, A. Ciabattoni, A. Petoukhova, et al., ESTRO IORT Task Force/ACROP recommendations for intraoperative radiation therapy with electrons (IOERT) in breast cancer, Radiother Oncol [Internet] 149 (2020 Aug 1) 150–157. https://pubmed.ncbi.nlm.nih.gov/32413529/.

[8] F.A. Calvo, J.M. Asencio, F. Roeder, R. Krempien, P. Poortmans, F.W. Hensley, et al., ESTRO IORT Task Force/ACROP recommendations for intraoperative radiation therapy in borderline-resected pancreatic cancer, Clin. Transl. Radiat. Oncol. 23 (2020) 91–99.

[9] F. Roeder, V. Morillo, L. Saleh-Ebrahimi, F.A. Calvo, P. Poortmans, Ferrer Albiach C. Intraoperative radiation therapy (IORT) for soft tissue sarcoma - ESTRO IORT Task Force/ACROP recommendations, Radiother Oncol. [Internet] 150 (2020 Sep 1) 293–302. https://pubmed.ncbi.nlm.nih.gov/32679306/.

[10] F.A. Calvo, C.V. Sole, H.J. Rutten, P. Poortmans, J.M. Asencio, J. Serrano, et al., ESTRO/ACROP IORT recommendations for intraoperative radiation therapy in primary locally advanced rectal cancer, Clin. Transl. Radiat. Oncol. 25 (2020 Nov 1) 29–36.

[11] C.V. Sole, F.A. Calvo, A. Polo, M. Cambeiro, C. Gonzalez, M. Desco, et al., Intraoperative electron-beam radiation therapy for pediatric ewing sarcomas and

rhabdomyosarcomas: long-term outcomes, Int. J. Radiat. Oncol. Biol. Phys. 92 (5) (2015 Aug 1) 1069–1076. http://www.redjournal.org/article/S0360301615004708/fulltext.
[12] O.W. Foley, J.A. Rauh-Hain, R.M. Clark, A. Goodman, W.B. Growdon, D.M. Boruta, et al., Intraoperative radiation therapy in the management of gynecologic malignancies, Am. J. Clin. Oncol. Cancer Clin. Trials [Internet] 39 (4) (2016 Aug 1) 329–334. https://journals.lww.com/amjclinicaloncology/Fulltext/2016/08000/Intraoperative_Radiation_Therapy_in_the_Management.3.aspx.
[13] M.S. Mendonca, W.T. Turchan, M.E. Day, C.N. Watson, N.C. Estabrook, H. Chin-Sinex, et al., (P003) delivery of ultra-rapid flash radiation therapy and demonstration of normal tissue sparing after abdominal irradiation of mice, Int. J. Radiat. Oncol. Biol. Phys. [Internet] 98 (2) (2017 Jun 1) E16. http://www.redjournal.org/article/S0360301617305047/fulltext.
[14] J. Bourhis, W.J. Sozzi, P.G. Jorge, O. Gaide, C. Bailat, F. Duclos, et al., Treatment of a first patient with FLASH-radiotherapy, Radiother Oncol. [Internet] 139 (2019 Oct 1) 18–22. http://www.thegreenjournal.com/article/S0167814019329597/fulltext.
[15] R.J. Griffin, M.M. Ahmed, B. Amendola, O. Belyakov, S.M. Bentzen, K.T. Butterworth, et al., Understanding high-dose, ultra-high dose rate, and spatially fractionated radiation therapy, Int. J. Radiat. Oncol. Biol. Phys. [Internet] 107 (4) (2020 Jul 15) 766–778. http://www.redjournal.org/article/S0360301620309585/fulltext.
[16] L.M.L. Smyth, J.F. Donoghue, J.A. Ventura, J. Livingstone, T. Bailey, L.R.J. Day, et al., Comparative toxicity of synchrotron and conventional radiation therapy based on total and partial body irradiation in a murine model, Sci. Rep. [Internet] 8 (1) (2018 Dec 1) 12044.
[17] M. Durante, E. BräUer-Krisch, M. Hill, Faster and safer? FLASH ultra-high dose rate in radiotherapy, Br. J. Radiol. [Internet] 91 (2018) 1082.
[18] P. Wilson, B. Jones, T. Yokoi, M. Hill, B. Vojnovic, Revisiting the ultra-high dose rate effect: implications for charged particle radiotherapy using protons and light ions, Br. J. Radiol. [Internet] 85 (1018) (2012 Oct) e933.
[19] Favaudon V, Caplier L, Monceau V, Pouzoulet F, Sayarath M, Fouillade C, et al., Ultrahigh dose-rate FLASH irradiation increases the differential response between normal and tumor tissue in mice, Sci. Transl. Med. 6 (245) (2014).
[20] P. Montay-Gruel, K. Petersson, M. Jaccard, G. Boivin, J.F. Germond, B. Petit, et al., Irradiation in a flash: unique sparing of memory in mice after whole brain irradiation with dose rates above 100 Gy/s, Radiother Oncol [Internet] 124 (3) (2017 Sep 1) 365–369. http://www.thegreenjournal.com/article/S0167814017303651/fulltext.
[21] J. Bourhis, P. Montay-Gruel, P. Gonçalves Jorge, C. Bailat, B. Petit, J. Ollivier, et al., Clinical translation of FLASH radiotherapy: why and how? Radiother Oncol [Internet] 139 (2019 Oct 1) 11–17. http://www.thegreenjournal.com/article/S0167814019303603/fulltext.
[22] M. Buonanno, V. Grilj, D.J. Brenner, Biological effects in normal cells exposed to FLASH dose rate protons, Radiother Oncol [Internet] 139 (2019 Oct 1) 51–55. http://www.thegreenjournal.com/article/S0167814019300763/fulltext.
[23] D.A. Simmons, F.M. Lartey, E. Schüler, M. Rafat, G. King, A. Kim, et al., Reduced cognitive deficits after FLASH irradiation of whole mouse brain are associated with less hippocampal dendritic spine loss and neuroinflammation, Radiother Oncol [Internet] 139 (2019 Oct 1) 4–10. http://www.thegreenjournal.com/article/S0167814019329421/fulltext.
[24] P. Montay-Gruel, M.M. Acharya, K. Petersson, L. Alikhani, C. Yakkala, B.D. Allen, et al., Long-term neurocognitive benefits of FLASH radiotherapy driven by reduced reactive oxygen species, Proc. Natl. Acad. Sci. U. S. A. 166 (22) (2019 May 28) 10943–10951.
[25] G. Felici, P. Barca, S. Barone, E. Bortoli, R. Borgheresi, S. De Stefano, et al., Transforming an IORT LINAC into a FLASH research machine: procedure and dosimetric characterisation, Front. Physiol. 8 (2020 Sep 11) 374.
[26] R. Moeckli, P. Gonçalves Jorge, V. Grilj, R. Oesterle, N. Cherbuin, J. Bourhis, et al., Commissioning of an ultra-high dose rate pulsed electron beam medical LINAC for FLASH RT preclinical animal experiments and future clinical human protocols, Med. Phys. [Internet] 48 (6) (2021 Jun 1) 3134–3142. https://onlinelibrary.wiley.com/doi/full/10.1002/mp.14885.
[27] Mobetron, Electron-beam IORT machine - IntraOp [internet]. https://intraop.com/mobetron-iort/.
[28] Soiort, S.I.T. Sordina IORT technologies S.p.A. [Internet]. https://www.soiort.com.
[29] S. Righi, E. Karaj, G. Felici, F. Di Martino, Dosimetric characteristics of electron beams produced by two mobile accelerators, Novac7 and liac, for intraoperative radiation therapy through Monte Carlo simulation, J. Appl. Clin. Med. Phys. 14 (1) (2013) 6–18.
[30] G. Iaccarino, L. Strigari, M. D'Andrea, L. Bellesi, G. Felici, A. Ciccotelli, et al., Monte Carlo simulation of electron beams generated by a 12 MeV dedicated mobile IORT accelerator, Phys. Med. Biol. [Internet] 56 (14) (2011 Jul 1) 4579. https://iopscience.iop.org/article/10.1088/0031-9155/56/14/022.
[31] H. Alhamada, S. Simon, C. Philippson, C. Vandekerkhove, Y. Jourani, N. Pauly, et al., 3D Monte Carlo dosimetry of intraoperative electron radiation therapy (IOERT), Phys. Med. [Internet] 57 (2019 Jan 1) 207–214. https://pubmed.ncbi.nlm.nih.gov/30738527/.
[32] I.J. Chetty, B. Curran, J.E. Cygler, J.J. DeMarco, G. Ezzell, B.A. Faddegon, et al., Report of the AAPM Task Group No. 105: issues associated with clinical implementation of Monte Carlo-based photon and electron external beam treatment planning, Med. Phys. [Internet] 34 (12) (2007) 4818–4853. https://pubmed.ncbi.nlm.nih.gov/18196810/.
[33] S.B. Jiang, A. Kapur, C.M. Ma, Electron beam modeling and commissioning for Monte Carlo treatment planning, Med. Phys. [Internet] 27 (1) (2000) 180–191. https://pubmed.ncbi.nlm.nih.gov/10659756/.
[34] J. Sempau, S.J. Wilderman, A.F. Bielajew, DPM, a fast, accurate Monte Carlo code optimised for photon and electron radiotherapy treatment planning dose calculations, Phys. Med. Biol. [Internet] 45 (8) (2000) 2263–2291. https://pubmed.ncbi.nlm.nih.gov/10958194/.
[35] F. Salvat, J.M. Fernández-Varea, Overview of physical interaction models for photon and electron transport used in Monte Carlo codes, Metrologia (2) (2009) 46.
[36] E.B. Podgorsak, IAEA Review of Radiation Oncology Physics - A HAndbook for Teachers and Students, International Atomic Energy Agency, Vienna, 2005.
[37] 2007 elastic Scattering of Electron and positrons, ICRU Report 77, 2007.
[38] S.M. Seltzer, M.J. Berger, Bremsstrahlung spectra from electron interactions with screened atomic nuclei and orbital electrons, Nucl. Instrum. Methods Phys. Res. Sect. B Beam Interact. Mater. Atoms 12 (1) (1985) 95–134.
[39] S.M. Seltzer, M.J. Berger, Bremsstrahlung energy spectra from electrons with kinetic energy 1 keV–10 GeV incident on screened nuclei and orbital electrons of neutral atoms with Z = 1–100, At Data Nucl. Data Tables 35 (3) (1986) 345–418.
[40] D. Sheikh-Bagheri, D.W.O. Rogers, Sensitivity of megavoltage photon beam Monte Carlo simulations to electron beam and other parameters, Med. Phys. [Internet] 29 (3) (2002) 379–390. https://pubmed.ncbi.nlm.nih.gov/11930913/.
[41] D. Sheikh-Bagheri, D.W.O. Rogers, Monte Carlo calculation of nine megavoltage photon beam spectra using the BEAM code, Med. Phys. [Internet] 29 (3) (2002) 391–402. https://pubmed.ncbi.nlm.nih.gov/11930914/.
[42] F. Verhaegen, C. Mubata, J. Pettingell, A.M. Bidmead, I. Rosenberg, D. Mockridge, et al., Monte Carlo calculation of output factors for circular, rectangular, and square fields of electron accelerators (6-20 MeV), Med. Phys. [Internet] 28 (6) (2001) 938–949. https://pubmed.ncbi.nlm.nih.gov/11439490/.
[43] Absorbed Dose Determination in External Beam Radiotherapy [Internet], (Technical Reports Series), INTERNATIONAL ATOMIC ENERGY AGENCY, Vienna, 2001. https://www.iaea.org/publications/5954/absorbed-dose-determination-in-external-beam-radiotherapy.